Optimization of Triangular Airfoils for Martian Helicopters using Direct Numerical Simulations

Lidia Caros *, Oliver Buxton †, Peter Vincent ‡
Imperial College London, London, England SW7 2AZ, United Kingdom

Mars has a lower atmospheric density than Earth, and the speed of sound is lower due to its atmospheric composition and lower surface temperature. Consequently, Martian rotor blades operate in a low-Reynolds-number compressible regime that is atypical for terrestrial helicopters. Non-conventional airfoils with sharp edges and flat surfaces have shown improved performance under such conditions, and second-order accurate Reynolds-Averaged Navier-Stokes (RANS) and Unsteady RANS (URANS) solvers have been combined with Genetic Algorithms to optimize them. However, flow over such airfoils is characterized by unsteady roll-up of coherent vortices which subsequently break down / transition. Accordingly, RANS/URANS solvers have limited predictive capability, especially at higher angles of attack where the aforementioned physics are more acute. To overcome this limitation, we undertake optimization using high-order Direct Numerical Simulations (DNS). Specifically, a triangular airfoil is optimized using DNS. Multi-objective optimization is performed to maximize lift and minimize drag, yielding a Pareto front. Various quantities including lift spectra and pressure distributions are analyzed for airfoils on the Pareto front to elucidate flow physics that yield optimal performance. The optimized airfoils that form the Pareto front achieve up to a 48% increase in lift or a 28% reduction in drag compared to a reference triangular airfoil studied in the Mars Wind Tunnel at Tohoku University. The work constitutes the first use of DNS for aerodynamic shape optimization.

I. Introduction

Throughout the last century, designers have worked to optimize airfoils for a wide range of terrestrial conditions. However, Martian atmospheric density is less than 1% of that on Earth, and Martian surface temperature and atmospheric composition lead to a lower speed of sound. Consequently, rotors for a Martian helicopter must operate in a low Reynolds number compressible regime that is seldom encountered on Earth, and for which conventional terrestrial airfoils have not been optimized.

The design of airfoils for Martian helicopters is a new and emerging field, recently catalyzed by the success of

*Doctoral Candidate, Department of Aeronautics, lidia.caros-roca19@imperial.ac.uk.
†Reader, Department of Aeronautics, o.buxton@imperial.ac.uk.
‡Professor, Department of Aeronautics, p.vincent@imperial.ac.uk.

Ingenuity, which flew on Mars for the first time in 2021 [1]. Studies by Munday et al. [2] and Konig et al. [3] have investigated the use of airfoils with sharp leading edges and flat surfaces that rely on unsteady lift generation mechanisms. These induce earlier separation compared to conventional airfoils, leading to an unsteady roll-up of coherent vortices on the suction side of the airfoil, which improves performance. Studies by Koning et al. [4] and Sasaki et al. [5] have also looked to optimize such airfoils by combining Reynolds-Averaged Navier Stokes (RANS) or unsteady RANS (URANS) solvers with Genetic Algorithms (GA). However, given the nature of the flow — which is unsteady, vortex-dominated, and transitional — RANS/URANS solvers have limited predictive capability, especially at higher angles of attack where the aforementioned flow physics are more acute [3, 4].

The current study overcomes this limitation by optimizing Martian airfoils using high-order accurate Direct Numerical Simulations (DNS). Specifically, a triangular airfoil is optimized at an angle of attack $\alpha = 12^\circ$ with a chord-based Reynolds number $Re = 3,000$ and Mach number $M = 0.15$ using three-dimensional (3D) DNS with periodic boundary conditions in the spanwise direction, via PyFR [6]. The chosen Reynolds number, Mach number and angle of attack α are representative of conditions at the root/mid-section of a rotor blade on a Martian helicopter. Flow physics associated with the optimal airfoils is analyzed, and compared with flow over a triangular airfoil previously studied by Munday et al. [2] and Caros et al. [7], henceforth referred to as the Reference Airfoil, to understand how the optimal airfoils achieve improved performance.

Sec. II details the methodology for the current work. Subsequently, Sec. III presents the results and analysis of the associated flow physics. Future work is presented in Sec. IV and finally conclusions are drawn in Sec. V.

II. Methodology

A. Optimization

1. Overview

A triangular airfoil is optimized at an angle of attack of $\alpha = 12^\circ$, a chord-based Reynolds number of $Re = 3000$, and a Mach number of $M = 0.15$, using 3D DNS with periodic boundary conditions in the spanwise direction. Genetic Algorithms (GA) [8] are used for the optimization. These algorithms are based on the theory of evolution and make use of genetic operators to advance towards the global optimum. Specifically, GAs explore the design space to find the fittest set of design variables for the given objective functions by evolving populations of individuals through generations. Although these algorithms require multiple evaluations to converge, they are considered suitable for problems with multiple objectives and nonlinear objective spaces with various local optima. Moreover, they do not require gradient information, which is challenging to obtain for the chaotic unsteady flow solutions produced by DNS. The particular GA used here is the Non-dominated Sorting Genetic Algorithm II (NSGA-II) by Deb et al. [9] implemented in Pymoo [10]; an open-source Python-based framework for single- and multi-objective optimization.

Figure 1 shows a flowchart of the optimization process. Prior to undertaking the 3D DNS optimization, a precursor two-dimensional (2D) DNS optimization is run, using 2D DNS to evaluate the objective functions. The result of the precursor 2D DNS optimization is then taken as the initial population for the 3D DNS optimization. Whilst it is well established that 2D DNS miss important flow physics when $\alpha = 12°$ [7], we anticipate that enough is retained such that using the result of the precursor 2D DNS optimization as the initial population for the 3D DNS optimization will accelerate convergence of the latter, and thus reduce the overall cost (since 2D DNS are of order 100× cheaper that 3D DNS).

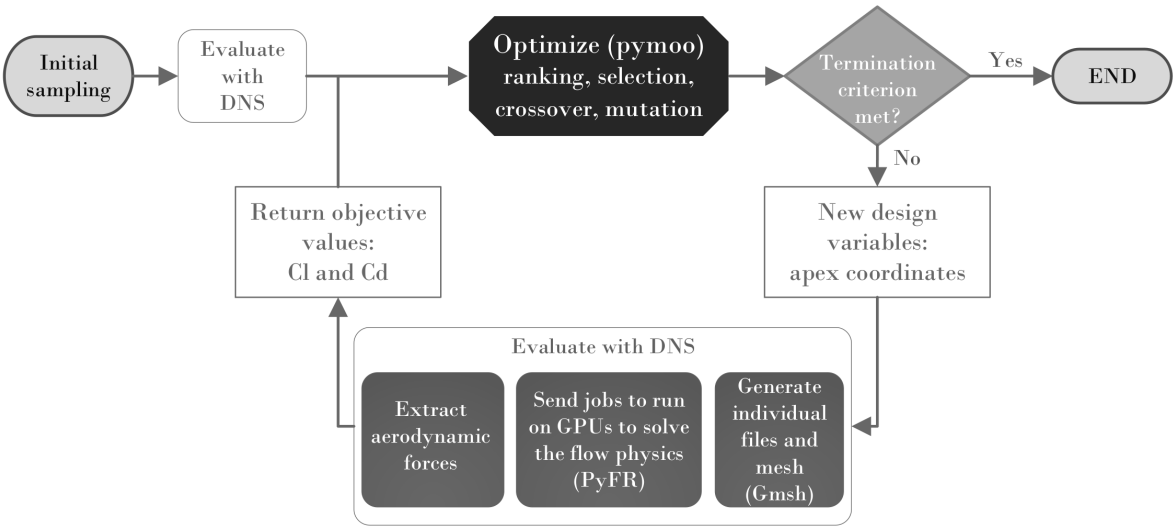

Fig. 1 Flowchart of optimization process.

2. Design variables and objective functions

The design variables are the x and y coordinates of airfoil apex, x_a and y_a, respectively, as shown in Figure 2. The coordinates are measured from the leading edge of the airfoil when $\alpha = 0°$. Design space constraints are applied such that

$$0.1 \leq x_a \leq 0.9, \qquad 0.02 \leq y_a \leq 0.4, \qquad y_a - x_a \leq 0, \qquad x_a + y_a - 1 \leq 0. \tag{1}$$

These avoid unfeasible/unrealistic geometries such as airfoils that are too thin to manufacture, or airfoils with very blunt leading/trailing edges, whilst retaining substantive coverage of the design space (see Figure 3).

The objective functions are the time-averaged lift coefficient, which is to be maximized, and the time-averaged drag coefficient, which is to be minimized.

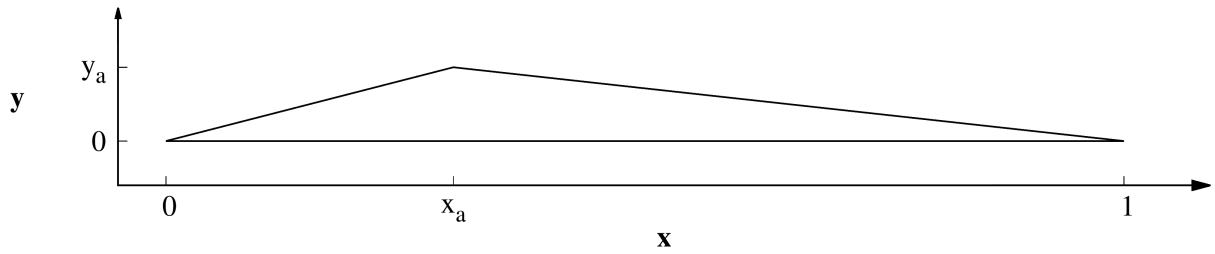

Fig. 2 Triangular airfoil with design variables x_a and y_a.

3. Optimization Parameters

The optimization begins with an initial population of individuals. Each individual is a set of apex coordinates representing an airfoil shape. The population size is constant, meaning that the optimum individuals of generation n might be replaced by better offspring from generation $n + 1$. The NSGA-II uses an elitist-preserving approach, meaning that the best individuals are not discarded, they are transferred directly to the next generation. This approach speeds up the performance of the GA significantly and helps prevent the loss of good solutions once they are found. The number of offspring determines how many new individuals are produced by the optimizer and evaluated at each generation. In this work, we have selected a population size of 30 individuals and 15 offspring based on the nature and availability of the computational resources. The environmental survival operator used in this work is Tournament Selection [11]. When generating the offspring, evolutionary operators (crossover and mutation) are applied to balance exploitation and exploration of the solution space. The operators used in this work are Simulated Binary Crossover [12] and Polynomial Mutation [12]. At each generation a restriction step is applied, in which any individuals violating the design space constraints were moved to the nearest point within the design space.

4. Initial Sampling

The initial population of the precursor 2D DNS optimization is obtained via a Latin Hypercube Sampling of the region $0 < x_a < 1, 0.02 < y_x < 0.4$, followed by a restriction step in which any individuals violating the design space constraints were moved to the nearest point within the design space.

Figure 3 shows the design space along with the initial population for the precursor 2D DNS optimization. The initial population of the 3D DNS optimization is the Pareto front at the 25th generation of the precursor 2D DNS optimization.

5. Termination and Convergence

The precursor 2D DNS optimization is terminated after 25 generations, and the 3D DNS optimization is terminated after 16 generations. Convergence is assessed using a hypervolume metric [13], which is calculated as the area dominated by the Pareto front at a particular generation with respect to a reference point. Hypervolume is a widely used performance metric [14] since it is Pareto compliant [15] and captures both convergence and diversity in a single

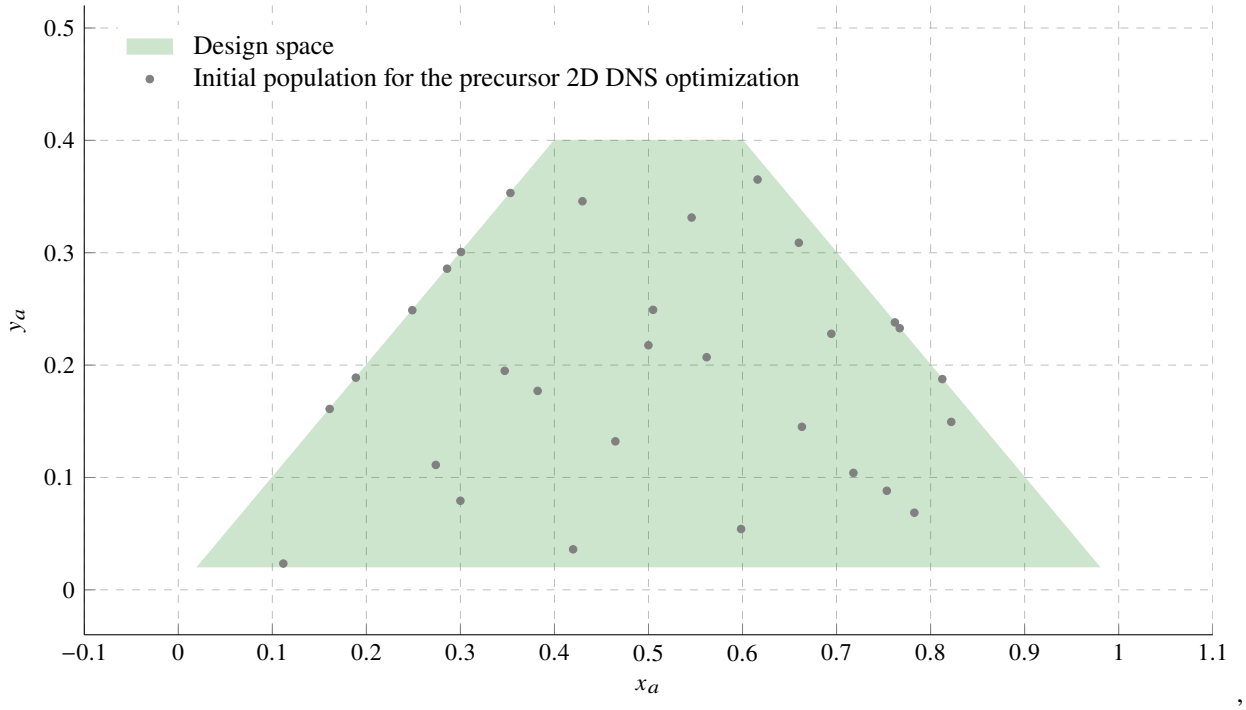

Fig. 3 Design space (green) along with initial population for the precursor 2D DNS optimization (grey dots).

value [16]. Figure 4 shows hypervolume, normalized by its value at the final generation, as a function of the number of generation for the precursor 2D DNS optimization and the 3D DNS optimization. Note how the 3D DNS optimization converges faster than the precursor 2D DNS optimization, since the former is seeded with the result of the latter.

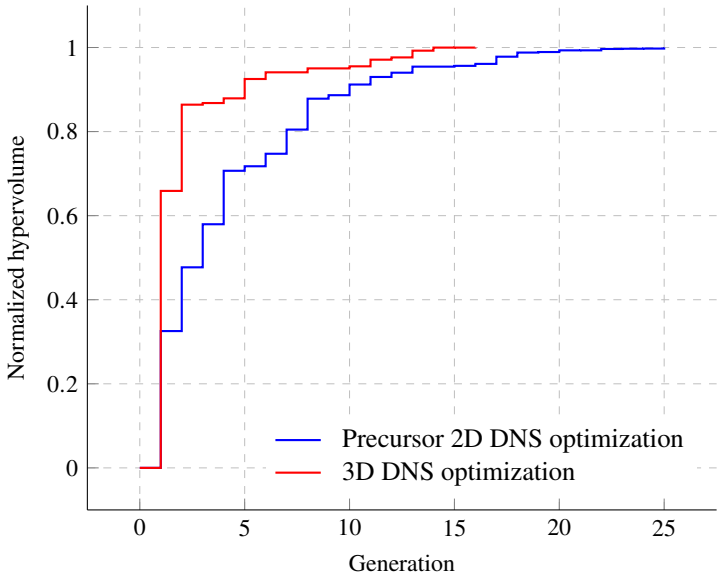

Fig. 4 Normalized hypervolume convergence as a function of the number of generations for the precursor 2D DNS optimization and the 3D DNS optimization, where the latter was initialized with the result of the former.

B. Objective Function Evaluation

1. Overview

The objective functions are the time-averaged lift and drag coefficients, which are evaluated by automatically meshing the geometry with Gmsh [17], solving the flow physics with PyFR [6], and extracting the time-averaged aerodynamic forces.

2. Governing Equations

PyFR [6] solves the compressible Navier-Stokes equations for an ideal gas with constant viscosity. These can be written in 3D as

$$\frac{\partial \mathbf{u}}{\partial t} + \boldsymbol{\nabla} \cdot \mathbf{f} = 0, \tag{2}$$

where $\mathbf{u} = \mathbf{u}(\mathbf{x}, t) = (\rho, \rho v_x, \rho v_y, \rho v_z, E)$ is the solution with ρ the fluid density, $\mathbf{v} = (v_x, v_y, v_z)$ the fluid velocity and E the total energy per unit volume, and where $\mathbf{f} = \mathbf{f}(\mathbf{u}, \boldsymbol{\nabla}\mathbf{u}) = \mathbf{f^i} - \mathbf{f^v}$ is the flux, with $\mathbf{f^i}$ the inviscid flux given by

$$\mathbf{f^i} = \begin{Bmatrix} \rho v_x & \rho v_y & \rho v_z \\ \rho v_x^2 + p & \rho v_y v_x & \rho v_z v_x \\ \rho v_x v_y & \rho v_y^2 + p & \rho v_z v_y \\ \rho v_x v_z & \rho v_y v_z & \rho v_z^2 + p \\ v_x(E+p) & v_y(E+p) & v_z(E+p) \end{Bmatrix}, \tag{3}$$

in which p is the pressure, which for an ideal gas is given by

$$p = (\gamma - 1)\left(E - \frac{1}{2}\rho \|\mathbf{v}\|^2\right), \tag{4}$$

with $\gamma = c_p/c_v$, where c_p and c_v are specific heat capacities at constant pressure and volume, respectively, and $\mathbf{f^v}$ is the viscous flux given by

$$\mathbf{f^v} = \begin{Bmatrix} 0 & 0 & 0 \\ \mathscr{T}_{xx} & \mathscr{T}_{yx} & \mathscr{T}_{zx} \\ \mathscr{T}_{xy} & \mathscr{T}_{yy} & \mathscr{T}_{zy} \\ \mathscr{T}_{xz} & \mathscr{T}_{yz} & \mathscr{T}_{zz} \\ v_i \mathscr{T}_{ix} + \Delta \partial_x T & v_i \mathscr{T}_{iy} + \Delta \partial_y T & v_i \mathscr{T}_{iz} + \Delta \partial_z T \end{Bmatrix}, \tag{5}$$

where the stress-energy tensor is given by

$$\mathscr{T}_{ij} = \mu(\partial_i v_j + \partial_j v_i) - \frac{2}{3}\mu\delta_{ij}\boldsymbol{\nabla}\cdot\mathbf{v}, \tag{6}$$

with μ the dynamic viscosity, $\Delta = \mu c_p/Pr$, with Pr the Prandtl number, and T is the static temperature, which for an ideal gas is given by

$$T = \frac{1}{c_v}\frac{1}{\gamma - 1}\frac{p}{\rho}. \tag{7}$$

In the current study values of $\gamma = 1.4$ and $Pr = 0.71$ were employed.

We note that the continuum approximation is valid when $M = 0.15$ and $Re = 3,000$ since the Knudsen number $K \approx M/\sqrt{Re} < 0.01$ [18, 19].

3. Solver and Numerical Method

PyFR is a cross-platform solver based on the high-order Flux Reconstruction approach of Huynh [20]. In the present work, fourth-order polynomials were used to represent the solution within each element of the mesh, thus nominally achieving fifth-order accuracy in space. A Rusanov Riemann solver was used to calculate the inter-element inviscid fluxes and the Local Discontinuous Galerkin approach was used to calculate the inter-element viscous fluxes. An explicit 5th stage 4th order Runge-Kutta time-stepping scheme, specifically version RK45[2R+] [21], with a fixed time-step was employed to advance the solution in time. These schemes are designed to have large time step stability limits, and have been widely adopted in a range of other high-order simulations [22, 23]. No anti-aliasing was employed, and all runs were performed using double-precision arithmetic. All simulations were undertaken using PyFR v1.15.0.

4. Computational Domain and Mesh

The triangular airfoils are defined to have a chord of 1.0 and infinitely sharp leading and trailing edges. The origin in the streamwise-vertical xy-plane is located at the leading edge of the airfoil when $\alpha = 0°$. The airfoil is rotated about its trailing edge to achieve an angle of attack of $\alpha = 12°$. The dimensions of the computational domain are $x \in [-10, 20]$ in the streamwise direction, $y \in [-10, 10]$ in the vertical direction and for the 3D DNS optimization $z \in [0, 0.6]$ in the spanwise direction. These dimensions are based on the computational study of Caros et al. [7], which shows that a spanwise extent of 0.6 chords is required in order to avoid constraining the breakdown of coherent vortices at angles of attack $\alpha > 7°$ for a triangular airfoil.

Gmsh [17] was used to automatically mesh the domain around each airfoil proposed by the optimizer. Gmsh is an open-source meshing tool that can be used to create unstructured meshes around complex geometries. A notable feature of Gmsh is that it can be scripted via a Python API.

In terms of topology, for the precursor 2D DNS optimization a structured quadrilateral mesh is located adjacent to

the airfoil surface, and an additional structured quadrilateral mesh is located in the wake region, extending a distance of 6.0 downstream of the airfoil. The remainder of the domain is then tessellated with an unstructured mix of quadrilaterals and triangles. For the 3D DNS optimization meshes are produced by extruding 2D meshes of the form described above by 18 elements in the span-wise z direction, generating hexahedra and triangular prisms throughout the domain. Figure 5 shows a streamwise-vertical xy-plane view of the mesh for the Reference Airfoil with $\alpha = 12°$.

In terms of element count, for the precursor 2D DNS optimization meshes had approximately $\sim 6 \times 10^3$ elements and $\sim 16 \times 10^3$ degrees of freedom per equation, and meshes for the 3D DNS optimization had $\sim 155 \times 10^3$ elements and $\sim 19.4 \times 10^6$ degrees of freedom per equation. These were similar to or greater than those used by Caros et al. [7] for the Reference Airfoil — which were themselves determined via a grid independence study, and were found to achieve good agreement with previously published DNS and experiments by Munday et al. [2]. Moreover, for four representative airfoils on the Pareto Front, DNS resolution was verified a posteriori in Appendix A. Specifically, it was determined that $3.5\eta > \Delta$ throughout the wake, where

$$\Delta = \frac{\sqrt[3]{V}}{p+1} \tag{8}$$

is an estimate of the local solution point spacing, with V the local element volume and p the polynomial order used to represent the solution within each element of the mesh, and

$$\eta = \left(\frac{\nu^3}{\varepsilon}\right)^{1/4} \tag{9}$$

is the Kolmogorov length scale, with ν the kinematic viscosity and

$$\varepsilon = 2\nu S_{ij} S_{ij} \tag{10}$$

the dissipation rate, where S_{ij} is the fluctuating rate-of-strain tensor. This is within the threshold required to achieve DNS resolution given the simulations are nominally fifth-order accurate in space [24].

5. Boundary conditions

A characteristic `char-riem-inv` PyFR boundary condition with density $\rho = 1.0$, velocity $\mathbf{v} = \{v_x, v_y, v_z\} = \{1.0, 0.0, 0.0\}$ and pressure $p = 31.746$, is applied at the $x = -10$ inflow, $x = 20$ outflow, $y = -10$ bottom, and $y = 10$ top boundaries to achieve $M = 0.15$ and $Re = 3,000$. An impermeable no-slip adiabatic `no-slp-adia-wall` PyFR boundary condition is applied at the airfoil surface. A periodic boundary condition is applied at the side planes. No turbulence is injected at the inflow.

Note that for an initial $5t_c$ of the 3D DNS, the velocity prescribed at the inflow plane is modified to have a

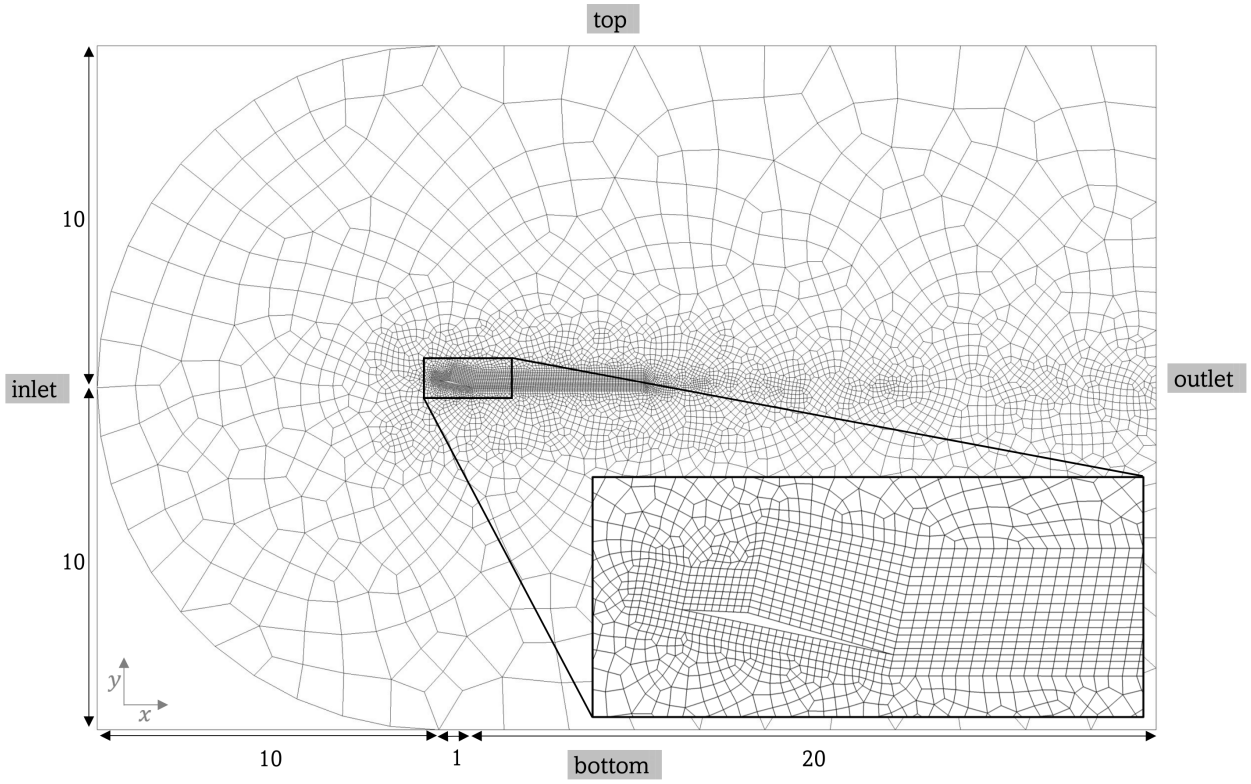

Fig. 5 Streamwise-vertical xy-plane view of mesh for the Reference Airfoil with $\alpha = 12°$. Reused with permission from L. Caros [7]. *Copyright 2022, Lidia Caros*.

time-dependent component as follows $\mathbf{v} = \{1 + 0.2\sin(100t), 0.2\sin(100t), 0.2\sin(100t)\}$ in order to trigger flow instabilities, with $t_c = 1.0/v_\infty$ where v_∞ is the free-stream velocity.

6. Data extraction

At $t = 0$, the simulations are initialized with uniform density $\rho = 1.0$, velocity $\mathbf{v} = \{v_x, v_y, v_z\} = \{1.0, 0.0, 0.0\}$ and pressure $p = 31.746$ throughout the domain. Simulations are advanced a period t_t to remove initial transients and then for a further t_e, henceforth referred to as the Data Extraction Period, during which data is extracted for analysis. For the precursor 2D DNS optimization $t_t = 50t_c$, $t_e = 50t_c$, and for the 3D DNS optimization $t_t = 75t_c$, $t_e = 75t_c$.

Instantaneous lift and drag coefficients are defined as

$$C_L = \frac{F_L}{q_\infty}, \qquad C_D = \frac{F_D}{q_\infty}, \tag{11}$$

respectively, where F_L and F_D are the instantaneous forces on the airfoil per unit area measured as the sum of viscous and pressure forces in the y and x directions, respectively, and q_∞ is obtained via

$$q_\infty = \frac{1}{2}\rho_\infty v_\infty^2 \tag{12}$$

where ρ_∞ is the free-stream density. Time-averaged lift and drag coefficients $\overline{C}_L$ and $\overline{C}_D$, can then be obtained by time-averaging C_L and C_D, respectively, over the Data Extraction Period.

Note that values for t_t and t_e were selected apriori for the precursor 2D DNS optimization and the 3D DNS optimization by manually analyzing the behaviour of C_L and C_D for each airfoil in each respective initial population. For reference, Figure 6 plots C_L as a function of time for a subset of nine airfoils from the initial population of the 3D DNS optimization. Moreover, the behaviour of C_L and C_D was manually analysed a posteriori for every airfoil to ensure t_t and t_e were suitable. However, we note that such a manual process may result in inefficiencies and/or potential averaging errors. Future work should investigate how to automatically determine t_t and t_e on-the-fly for each simulation as per Bergmann et al. [25].

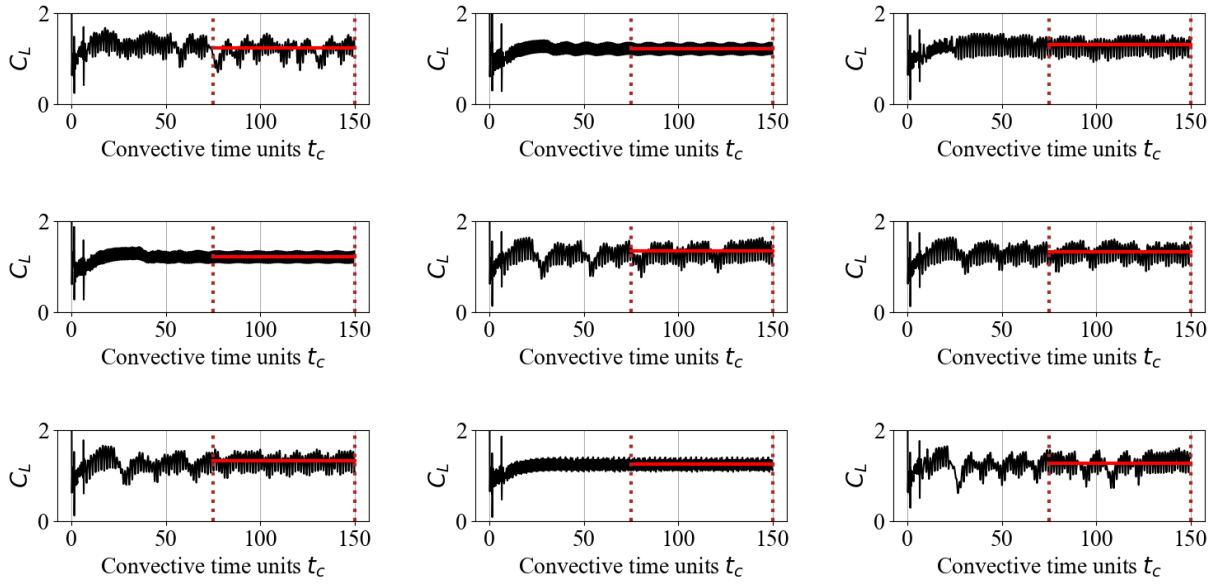

Fig. 6 C_L as a function of time for a subset of 9 airfoils from the initial population of the 3D DNS optimization. The horizontal red line marks $\overline{C}_L$. The vertical dotted lines mark the start and end of the Data Extraction Period.

C. Deployment and Costs

The optimization was performed on Piz Daint at the Swiss National Supercomputing Centre (CSCS). Pymoo and Gmsh were invoked on the login node (Intel Xeon E5-2650 v3 2.30GHz CPU) via Bash scripts, PyFR was invoked on the compute nodes (Tesla P100-16GB GPUs). The precursor 2D DNS optimization was run for 25 generations, with 15 individuals in each generation except for the first, which had 30 individuals. Each of the 2D DNS took approximately 2 hours to run on 1 Tesla P100-16GB GPU, therefore, the precursor 2D DNS optimization required approximately 780 GPUhs. The 3D DNS optimization was run for 16 generations, with 15 individuals in each generation except for the first, which had 30 individuals. Each of the 3D DNS took approximately 23 hours to run on 36 Tesla P100-16GB GPUs,

therefore, the 3D DNS optimization required approximately 88,000 GPUhs. Note that the 3D DNS were run on 15 Tesla P100-16GB GPUs in order to achieve a run time below 24h, which is the maximum job duration limit on Piz Daint. This avoided re-queuing to complete a given run. In total, the overall cost of the optimization was ~ 200,000 GPUhs.

III. Results

A. Optimal airfoils

Figure 7a plots apex locations in the x_a, y_a design space for the optimal airfoils from the 15th generation of the final 3D DNS optimization, along with the apex location for the Reference Airfoil. The optimal airfoils are thicker than the Reference Airfoil, and their apexes are shifted downstream. Figure 7b plots the Pareto front of optimal airfoils in the $\overline{C}_L$, $\overline{C}_D$ objective space from the 15th generation of the final 3D DNS optimization. All the airfoils on the Pareto front have improved $\overline{C}_L$ and $\overline{C}_D$ compared to the Reference Airfoil. Specifically, $\overline{C}_L$ is increased by up to 48% and $\overline{C}_D$ is reduced by up to 28%.

Based on associated flow characteristics, four distinct groups of airfoils can be identified on the Pareto front, defined as per Table 1. A detailed discussion of the flow physics associated with each group, including analysis of Q-criterion isosurfaces, lift coefficient C_L, time-averaged pressure coefficient $\overline{C}_p$, time-averaged velocity line integral convolutions (LICs) and time-averaged skin friction $\overline{C}_f$, is presented below.

Group	$\overline{\mathbf{C}}_\mathbf{L}$ and $\overline{\mathbf{C}}_\mathbf{D}$	**Spanwise breakdown**	C_L **temporal behaviour**	$\overline{C}_p$ **distribution**	$\overline{C}_f$ **distribution**
1	Lowest	Rib-roller vortex structure	Low amplitude with dominant freq. St ≈ 1.1	Plateau with early fall	Change of sign at trailing edge
2	Intermediate	Rib-roller vortex structure	Low amplitude with dominant freq. St ≈ 1.1	Plateau with later fall	Change of sign at apex and trailing edge
3	Intermediate	Spanwise unstructured	High amplitude with dominant freq. St ≈ 0.65	Plateau with later fall	Change of sign at apex and trailing edge
4	Highest	Spanwise unstructured	High amplitude with dominant freq. St ≈ 0.65	Plateau with later fall	Change of sign at trailing edge
Reference Airfoil	-	Spanwise unstructured	High amplitude with dominant freq. St ≈ 1.1 and energy content at low freq.	Plateau with smooth fall and lower suction	Change of sign at trailing edge and weaker recirculation

Table 1 Flow characteristics associated with each of the four distinct groups of airfoils on the Pareto front, along with flow characteristics associated with the Reference Airfoil.

B. Q-criterion Isosurfaces and Lift Coefficient

Figure 8 shows, for a representative airfoil of each group and the Reference Airfoil, instantaneous Q-criterion isosurfaces colored by velocity magnitude $|v|$ (left), C_L time series for the Data Extraction Period (middle) and C_L

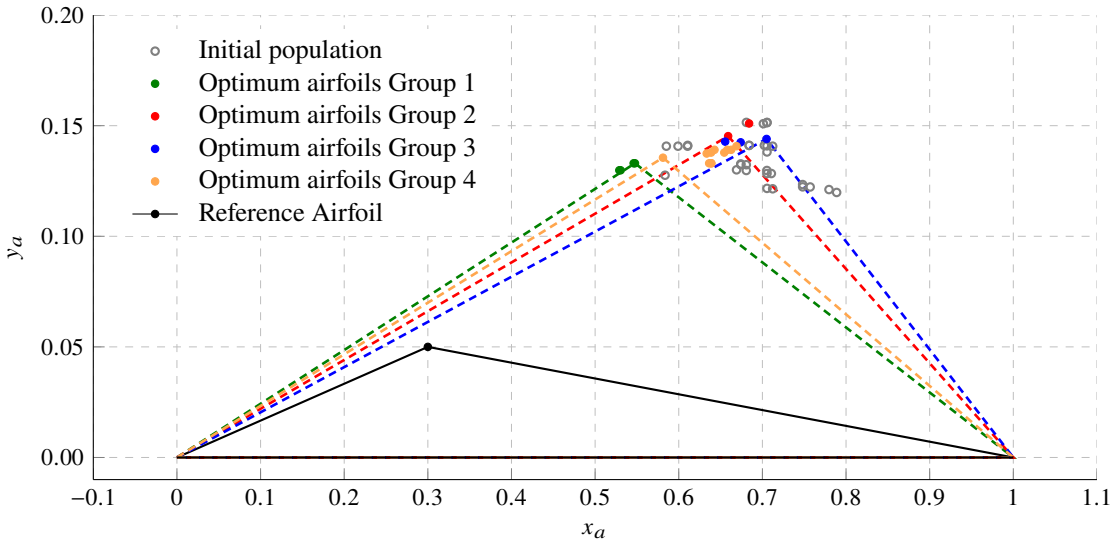

(a)

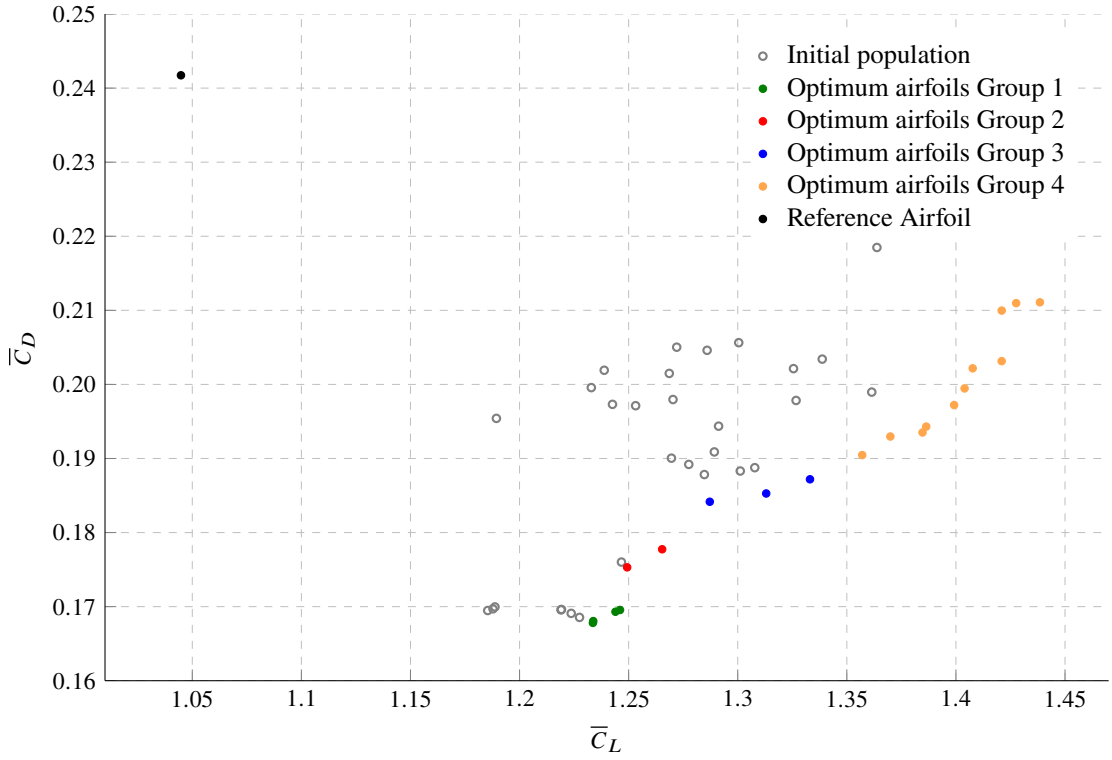

(b)

Fig. 7 Plots of x_a, y_a for the initial population (hollow circles), and optimal airfoils (solid circles), for the 3D DNS optimization (a). Plots of $\overline{C}_L$, $\overline{C}_D$ for the initial population (hollow circles), and optimal airfoils (solid circles), forming the Pareto front, for the 3D DNS optimization (b). Optimal airfoils are from the 15th generation of the 3D DNS optimization.

spectra for the Data Extraction Period (right).

The Q-criterion isosurfaces show the inherently unsteady nature of the flow over all airfoils, with separation from the

sharp leading edge and subsequent roll-up of large coherent structures on the suction side of the airfoils. In all cases, the flow breaks down in the spanwise direction and becomes three-dimensional. For Groups 1 and 2, it is easy to identify the rib-roller vortex structure in the wake, typical of a mixing layer [26], with periodically repeating cells of span ~0.3 chords. For Groups 3 and 4, the breakdown is unstructured, with no repeating spanwise structures. The C_L time series also reflect the unsteadiness of the flow that is characteristic of these sharp-leading-edge airfoils, with large-amplitude oscillations corresponding to the vortex roll-up. Groups 1 and 2 show lower amplitude fluctuations than Groups 3 and 4. A correlation between large amplitude fluctuations and high $\overline{C}_L$ can be identified from the plots, with Groups 3 and 4 having the highest of both. The spectra show the dominant frequencies of the C_L time series for the representative airfoils of each group. Groups 1 and 2 have a dominant frequency at $St \approx 1.1$, while Groups 3 and 4 have a dominant frequency at $St \approx 0.6$. The Reference Airfoil induces similar flow behaviour to Groups 3 and 4 in terms of span-wise breakdown and C_L time series. However, its dominant frequency of $St \approx 1.1$ is closer to that of Groups 1 and 2.

C. Pressure Coefficient Distribution

Time-averaged pressure coefficient $\overline{C}_p$ is defined as

$$\overline{C}_p = \frac{\overline{p} - p_\infty}{q_\infty} \tag{13}$$

where $\overline{p}$ is the time-averaged static pressure, p_∞ is the free-stream static pressure and q_∞ is the free-stream dynamic pressure obtained via Eq. (12). Figure 9 plots mid-span $\overline{C}_p$ distributions on the surface of a representative airfoil from each group on the Pareto front, and the Reference Airfoil, as a function of $\tilde{x} = x/a$, where a is the x-wise distance between the leading and trailing edge of the airfoil. The vertical dashed lines show the position of the apex for each airfoil.

The optimal airfoils exhibit a region of lower $\overline{C}_p$ above the upstream portion of the suction surface, followed by a downstream pressure recovery region, which is typical of a laminar separation bubble [27–30]. Specifically, $\overline{C}_p$ remains broadly constant over the upstream portion of the suction surface. There is then a rapid pressure recovery region immediately upstream of the apex, followed by a final slower recovery region downstream of the apex; although in all cases $\overline{C}_p$ does not fully recover to the free-stream value prior to the trailing edge.

The Reference Airfoil exhibits a relatively much flatter $\overline{C}_p$ distribution over the suction surface of the airfoil, attaining significantly higher $\overline{C}_p$ than the optimal airfoils over the upstream portion of the suction surface, but a slightly lower value over the downstream portion of the suction surface.

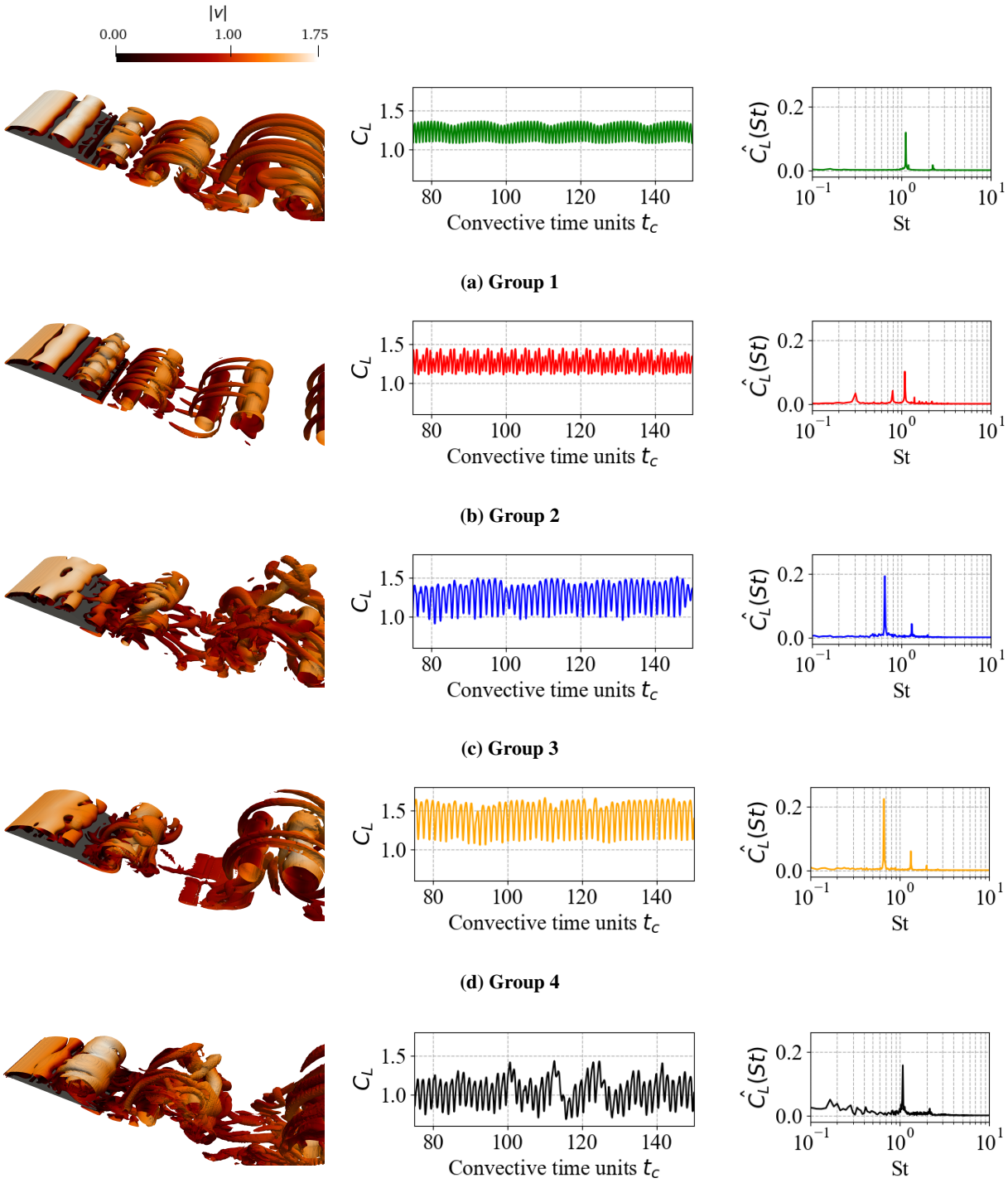

(a) Group 1

(b) Group 2

(c) Group 3

(d) Group 4

(e) Reference Airfoil

Fig. 8 Instantaneous Q-criterion isosurfaces colored by velocity magnitude $|v|$ (left), C_L time-series (middle) and C_L spectra (right) for one representative airfoil of each group on the Pareto front and the Reference Airfoil.

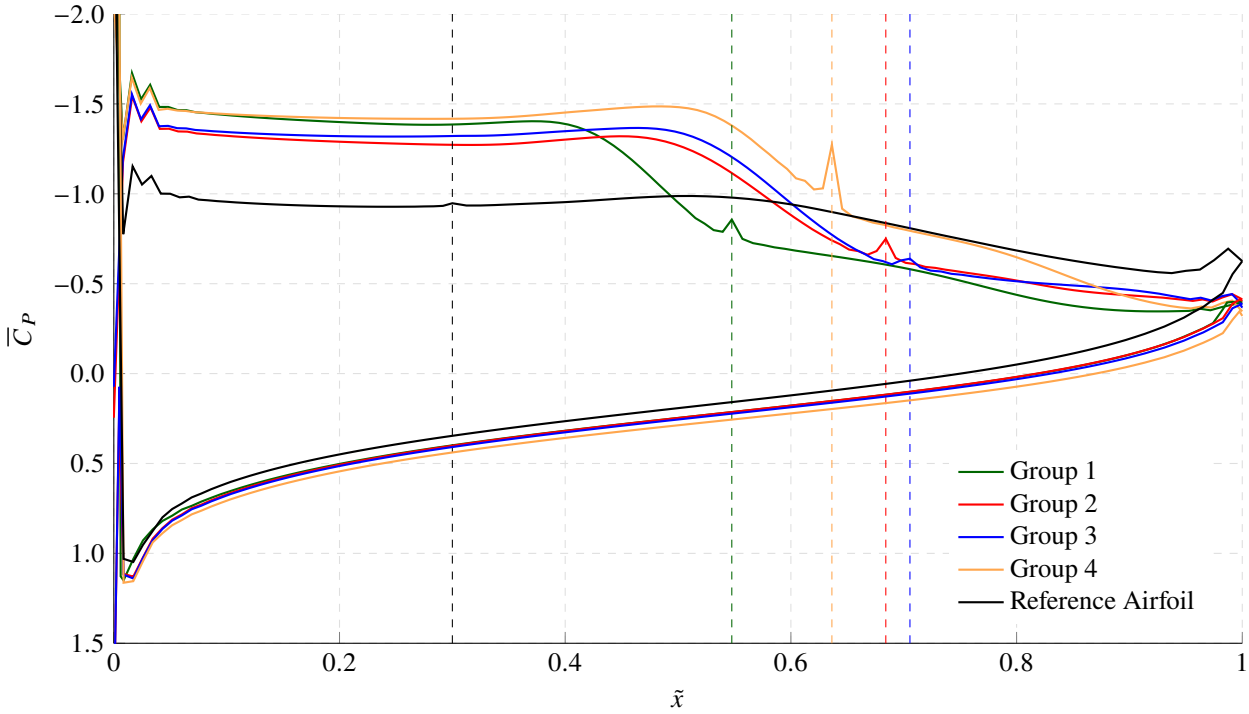

Fig. 9 Plots of mid-span $\overline{C}_p$ distributions on the surface of a representative airfoil from each group on the Pareto front, and the Reference Airfoil, as a function of $\tilde{x}$. The dashed lines show the position of the apex for each airfoil.

D. Velocity Line Integral Convolutions (LICs) and Skin Friction Distribution

The time-averaged skin friction coefficient $\overline{C}_f$ is defined as

$$\overline{C}_f = \frac{\overline{\tau}_s}{q_\infty} \tag{14}$$

where $\overline{\tau}_s$ is the stream-wise component of the time-averaged wall shear stress and q_∞ is obtained via Eq. (12).

Figure 10 plots time-averaged velocity magnitude $|v|$ in a span-wise constant plane, with superimposed time-averaged velocity Line Integral Convolutions (LICs) [31] (left), and $\overline{C}_f$ distributions on the suction surface as a function of $\tilde{x}$ (right), for a representative airfoil from each group on the Pareto front, and the Reference Airfoil. The dashed lines show the position of the apex for each airfoil.

For the optimal airfoils, the LIC plots show two large recirculation regions adjacent to the suction surface, which are responsible for the increased lift. The recirculation regions can also be identified from the two pronounced negative peaks in the $\overline{C}_f$ distributions. Airfoils in Groups 2 and 3 experience a change in sign of $\overline{C}_f$ near the apex, which signifies reattachment in the time-averaged sense. The flow then separates again downstream of the apex, with vortices rolling up on the downstream suction surface of the airfoil. Airfoils in Groups 1 and 4 show a similar $\overline{C}_f$ distribution to those in Groups 2 and 3, but without reattachment; they induce separated flow, in the time-averaged sense, for the

entirety of the chord. All the airfoils induce a change of sign of $\overline{C}_f$ near the trailing edge due to the vortex generated by the flow coming from the pressure surface being sucked upwards to the suction surface.

The Reference Airfoil exhibits fully separated flow from the leading edge with a recirculation region further downstream and further away from the suction surface compared to the optimum airfoils. Consequently, the Reference Airfoil is unable to create such a strong overall suction effect, as observed in the $\overline{C}_p$ distribution in Fig. 9.

E. Summary

The airfoils on the Pareto front achieve optimal performance by exploiting vortex roll-up as a lifting mechanism. Specifically, they aim to retain a strong vortex close to the upstream portion of the suction surface, prior to the apex, whilst avoiding excessive inclination of the downstream portion of the suction surface, which would result in a high pressure drag. This is achieved by positioning their apexes downstream of $x \approx 0.5$ and at $y \approx 0.15$; setting the upstream portion of the suction surface approximately parallel to the free-stream flow when $\alpha = 12°$.

Airfoils in Group 1 have the lowest $\overline{C}_L$ values, since their apexes are upstream of those in Groups 2, 3 and 4, which reduces the extent of the low-pressure region on the upstream portion of the suction surface (see Fig. 9 and Fig. 10). Group 1 airfoils also have the lowest $\overline{C}_D$ values, likely because the downstream portion of their upper surface is less steeply inclined (see Fig. 7a). Airfoils in this Group exhibit a rib-roller vortex structure with a low amplitude C_L fluctuations and a dominant frequency at $St = 1.1$.

Airfoils in Groups 2 and 3 are in the middle of the Pareto front, with intermediate values of $\overline{C}_L$ and $\overline{C}_D$. The airfoils in these groups are characterized by reattachment of the flow near the apex in the time-averaged sense (see Fig. 10). They have intermediate values of $\overline{C}_L$ and $\overline{C}_D$ because the low-pressure region on the upstream portion of their suction surface is larger than for Group 1, but therir vortices roll-up further from the suction surface compared to Group 4 (see Fig. 9 and Fig. 10). Groups 2 and 3 differ in their vortex structures and C_L behaviour, with airfoils in Group 2 having a rib-roller vortex structure with low-amplitude C_L fluctuations and a dominant frequency at $St = 1.1$, similar to Group 1, whereas Group 3 airfoils show higher values of $\overline{C}_L$ and $\overline{C}_D$ compared to those in Group 2, and they exhibit an unstructured spanwise breakdown, with high-amplitude C_L fluctuations and a dominant frequency at $St = 0.65$.

Finally, airfoils in Group 4 have the highest values of $\overline{C}_L$ and $\overline{C}_D$ because the low-pressure region on the upstream portion of their suction surface is larger than for Group 1, and their vortices roll-up closer to the suction surface compared to Groups 2 and 3. Airfoils in this Group exhibit similar flow structures and C_L behaviour to those in Group 3, with an unstructured spanwise breakdown, high amplitude C_L fluctuations and a dominant frequency at $St = 0.65$.

IV. Future Work

Airfoils with sharp edges can be very sensitive to flow instabilities such as incoming turbulence, especially when the flow is separating from the sharp leading edge, and when the flow experiences reattachment. Since these airfoils

are being optimized for use on helicopter blades, their inflow conditions will most likely be affected by ambient turbulence and the wake of the previous blade. Future work should investigate the effect of incoming turbulence and/or inflow-outflow periodicity on the optimization of triangular airfoils. Also, the edges of the airfoils in the current work are infinitely sharp, which is unrealistic when considering fabrication tolerances. Thus, performance of the optimal airfoils should be assessed after rounding the edges, since it may have an effect on how flow separates. In terms of the optimization, the angle of attack should be added as a design variable, and more complex shapes should be investigated, as well as tradeoffs around structural realisability and weight. Finally, further convergence acceleration strategies should be explored to reduce the cost of 3D DNS optimization, such as the use of surrogate models.

V. Conclusions

A triangular airfoil has been optimized at an angle of attack $\alpha = 12°$ with a chord-based $Re = 3,000$ and Mach number $M = 0.15$ using 3D DNS with periodic boundary conditions in the spanwise direction via PyFR. The chosen Reynolds number, Mach number and angle of attack α are representative of conditions at the root/mid-section of a rotor blade on a Martian helicopter. Specifically, multi-objective optimization was performed to maximize lift and minimize drag, yielding a Pareto front of non-dominated airfoils. Q-criterion isosurfaces, lift coefficient spectra, pressure coefficient distributions, velocity line integral convolutions and skin friction distributions were analyzed for airfoils on the Pareto front to elucidate the flow physics that yield optimal performance. It was found that the optimal airfoils exploit vortex roll-up as a lifting mechanism. Specifically, they aim to retain a strong vortex close to the upstream portion of the suction surface, prior to the apex, whilst avoiding excessive inclination of the downstream portion of the suction surface, which would result in a high pressure drag. This is achieved by positioning their apexes downstream of $x \approx 0.5$ and at $y \approx 0.15$; setting the upstream portion of the suction surface approximately parallel to the free-stream flow when $\alpha = 12°$. The optimized airfoils that form the Pareto front achieve up to a 48% increase in lift or a 28% reduction in drag compared to the Reference Airfoil. The work constitutes the first use of DNS for aerodynamic shape optimization.

Appendix A

3D DNS for a representative airfoil from each group was re-started from $t = 150t_c$ and run for a further $400t_c$, during which data was extracted for analysis. Figures 11, 12, 13 and 14 show plots of Δ/η along various mid-span lines for the representative airfoils from Groups 1, 2, 3 and 4, respectively, where Δ is an estimate of the solution point spacing given by Eq. (8) and η is an estimate of the Kolmogorov length scale given by Eq. (9).

Acknowledgements

The authors are grateful for support from the Engineering and Physical Sciences Research Council via an EPSRC Fellowship (EP/R030340/1) and compute allocations on Cirrus at the Edinburgh Parallel Computing Centre (EPCC) and Piz Daint at the Swiss National Supercomputing Centre (CSCS).

References

[1] Balaram, J. B., Canham, T., Duncan, C., Golombek, M., Grip, H. F., Johnson, W., Maki, J., Quon, A., Stern, R., and Zhu, D., "Mars helicopter technology demonstrator," *AIAA Atmospheric Flight Mechanics Conference*, 2018. https://doi.org/10.2514/6.2018-0023.

[2] Munday, P., Taira, K., Suwa, T., Numata, D., and Asai, K., "Non-linear lift on a triangular airfoil in low-Reynolds-number compressible flow," *Journal of Aircraft*, Vol. 52, 2015, pp. 924–931. https://doi.org/10.2514/1.C032983.

[3] Koning, W. J., Romander, E. A., and Johnson, W., "Performance optimization of plate airfoils for Martian rotor applications using a genetic algorithm," *45th European Rotorcraft Forum 2019, ERF 2019*, Vol. 1, 2019.

[4] Koning, W. J. F., Romander, E. A., and Johnson, W., "Optimization of low Reynolds number airfoils for Martian rotor applications using an evolutionary algorithm," *AIAA Science and Technology Forum and Exposition (AIAA SciTech)*, 2020. https://doi.org/10.2514/6.2020-0084.

[5] Sasaki, G., Tatsukawa, T., Nonomura, T., Oyama, A., Matsumoto, T., and Yonemoto, K., "Multi-objective optimization of airfoil for Mars exploration aircraft using genetic algorithm," *Transactions of the Japan Society for Aeronautical and Space Sciences, Aerospace Technology Japan*, Vol. 12, 2014, pp. 59–64. https://doi.org/10.2322/tastj.12.Pk_59.

[6] Witherden, F., Farrington, A., and Vincent, P., "PyFR: An Open Source Framework for Solving Advection-Diffusion Type Problems on Streaming Architectures using the Flux Reconstruction Approach," *Computer Physics Communications*, Vol. 185, 2014, pp. 3028–3040. https://doi.org/10.1016/j.cpc.2014.07.011.

[7] Caros, L., Buxton, O., Shigeta, T., Nagata, T., Nonomura, T., Asai, K., and Vincent, P., "Direct numerical simulation of flow over a triangular airfoil under Martian conditions," *AIAA Journal*, 2022. https://doi.org/10.2514/1.J061454.

[8] Goldberg, D., *Genetic Algorithm in Search, Optimization, and Machine Learning*, Vol. XIII, Addison-Wesley Longman Publishing Co., Inc., 1989.

[9] Kalyanmoy, D., Sameer, A., and Meyarivan, T., "A fast elitist non-dominated sorting genetic algorithm for multi-objective optimization NSGA-II," *IEEE Transaction on Evolutionary Compution*, Vol. 6, 2002, pp. 182–197. https://doi.org/10.1007/3-540-45356-3_83.

[10] Blank, J., and Deb, K., "Pymoo: multi-objective optimization in Python," *IEEE Access*, Vol. PP, 2020, pp. 1–1. https://doi.org/10.1109/ACCESS.2020.2990567.

[11] Goldberg, D. E., and Deb, K., "A Comparative Analysis of Selection Schemes Used in Genetic Algorithms," , 1991. https://doi.org/10.1016/b978-0-08-050684-5.50008-2.

[12] Deb, K., Sindhya, K., and Okabe, T., "Self-adaptive simulated binary crossover for real-parameter optimization," *Proceedings of GECCO 2007: Genetic and Evolutionary Computation Conference*, 2007. https://doi.org/10.1145/1276958.1277190.

[13] Zitzler, E., and Thiele, L., "Multiobjective optimization using evolutionary algorithms - A comparative case study," *Lecture Notes in Computer Science*, Vol. 1498 LNCS, 1998. https://doi.org/10.1007/bfb0056872.

[14] Riquelme, N., Lücken, C. V., and Barán, B., "Performance metrics in multi-objective optimization," 2015. https://doi.org/10.1109/CLEI.2015.7360024.

[15] Zitzler, E., Brockhoff, D., and Thiele, L., "The hypervolume indicator revisited: On the design of pareto-compliant indicators via weighted integration," *Lecture Notes in Computer Science*, Vol. 4403 LNCS, 2007. https://doi.org/10.1007/978-3-540-70928-2_64.

[16] Simpson, T. W., Mauery, T. M., Korte, J. J., and Mistree, F., "Comparison of response surface and kriging models for multidisciplinary design optimization," *7th AIAA USAF NASA ISSMO Symposium on Multidisciplinary Analysis and Optimization*, 1998. https://doi.org/10.2514/6.1998-4755.

[17] Geuzaine, C., and Remacle, J. F., "Gmsh: A 3-D finite element mesh generator with built-in pre- and post-processing facilities," *International Journal for Numerical Methods in Engineering*, Vol. 79, 2009. https://doi.org/10.1002/nme.2579.

[18] Pekardan, C., and Alexeenko, A., "Rarefaction effects for transonic airfoil flows at low reynolds numbers," *AIAA Journal*, Vol. 56, No. 2, 2018. https://doi.org/10.2514/1.J056051.

[19] Hoerner, S. F., *Fluid-dynamic drag*, Published by the Author, Bakersfield, CA 93390, 1965.

[20] Huynh, H., "A flux reconstruction approach to high-order schemes including discontinuous Galerkin methods," *AIAA Paper 4079*, 2007, pp. 1–42.

[21] Kennedy, C. A., Carpenter, M. H., and Lewis, R. M., "Low-storage, explicit Runge-Kutta schemes for the compressible Navier-Stokes equations," *Applied Numerical Mathematics*, Vol. 35, No. 3, 2000, pp. 177–219. https://doi.org/10.1016/S0168-9274(99)00141-5.

[22] Vincent, P., Witherden, F., Vermeire, B., Park, J. S., and Iyer, A., "Towards Green Aviation with Python at Petascale," *SC '16: Proceedings of the International Conference for High Performance Computing, Networking, Storage and Analysis*, 2016, pp. 1–11. https://doi.org/10.1109/SC.2016.1.

[23] Park, J. S., Witherden, F. D., and Vincent, P. E., "High-order implicit large-eddy simulations of flow over a NACA0021 aerofoil," *AIAA Journal*, Vol. 55, No. 7, 2017. https://doi.org/10.2514/1.J055304.

[24] Buxton, O., Laizet, S., and Ganapathisubramani, B., "The effects of resolution and noise on kinematic features of fine-scale turbulence," *Experiments in Fluids*, Vol. 51, No. 5, 2011, pp. 1417–1437. https://doi.org/10.1007/s00348-011-1159-2.

[25] Bergmann, M., Morsbach, C., Ashcroft, G., and Kugeler, E., "Statistical Error Estimation Methods for Engineering-Relevant Quantities From Scale-Resolving Simulations," *Journal of Turbomachinery*, Vol. 144, 2022. https://doi.org/10.1115/1.4052402.

[26] Rogers, M. M., and Moser, R. D., "The three-dimensional evolution of a plane mixing layer: The Kelvin-Helmholtz rollup," *Journal of Fluid Mechanics*, Vol. 243, 1992, pp. 183–226. https://doi.org/10.1017/S0022112092002696.

[27] Lin, J. C., and Pauley, L. L., "Low-Reynolds-number separation on an airfoil," *AIAA Journal*, Vol. 34, 1996. https://doi.org/10.2514/3.13273.

[28] Counsil, J. N., and Boulama, K. G., "Low-reynolds-number aerodynamic performances of the NACA 0012 and Selig-Donovan 7003 airfoils," *Journal of Aircraft*, Vol. 50, 2013. https://doi.org/10.2514/1.C031856.

[29] Genc, I. K. M. S., "Numerical Study on Low Reynolds Number Flows Over an Aerofoil," *Journal of Applied Mechanical Engineering*, Vol. 02, 2013. https://doi.org/10.4172/2168-9873.1000131.

[30] Anyoji, M., Nonomura, T., Aono, H., Oyama, A., Fujii, K., Nagai, H., and Asai, K., "Computational and experimental analysis of a high-performance airfoil under low-reynolds-number flow condition," *Journal of Aircraft*, Vol. 51, 2014. https://doi.org/10.2514/1.C032553.

[31] Cabral, B., and Leedom, L., "Imaging vector fields using line integral convolution," 1993. https://doi.org/10.1145/166117.166151.

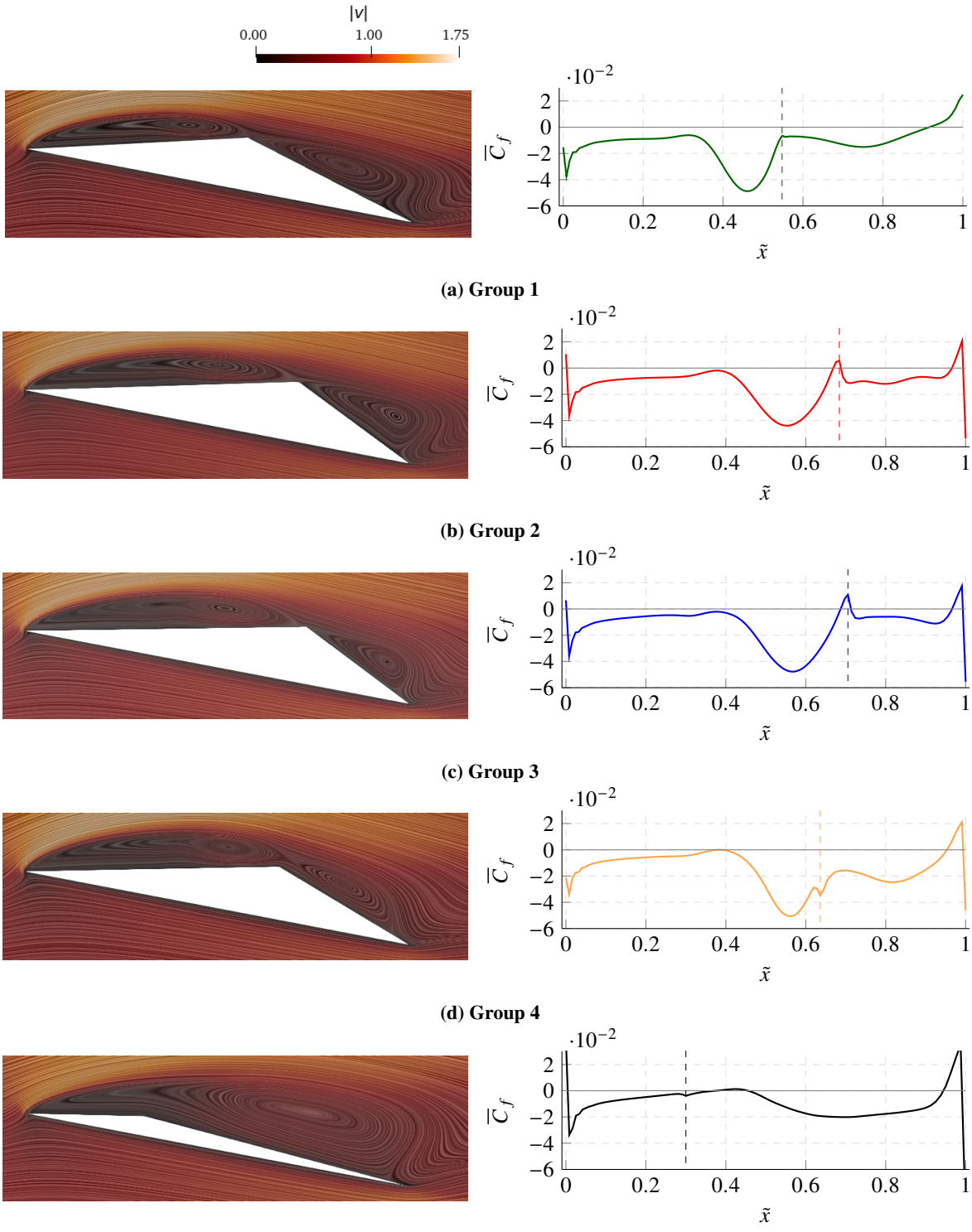

(a) Group 1

(b) Group 2

(c) Group 3

(d) Group 4

(e) Reference Airfoil

Fig. 10 Time-averaged velocity magnitude $|v|$ in a span-wise constant plane, with superimposed time-averaged velocity LICs (left), and mid-span $\overline{C}_f$ distributions on the suction surface as a function of $\tilde{x}$ (right), for a representative airfoil from each group on the Pareto front, and the Reference Airfoil. The dashed lines show the position of the apex for each airfoil.

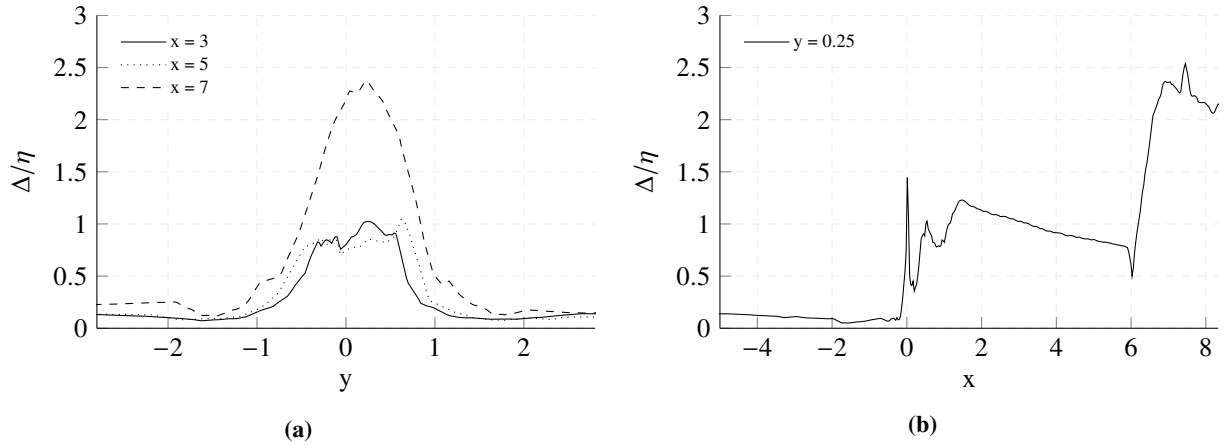

(a) (b)

Fig. 11 Plots of Δ/η in the mid-span plane as a function of y at x = 3, x = 5 and x = 7 (a) and as a function of x at y = 0.2 (b) for a representative airfoil from Group 1.

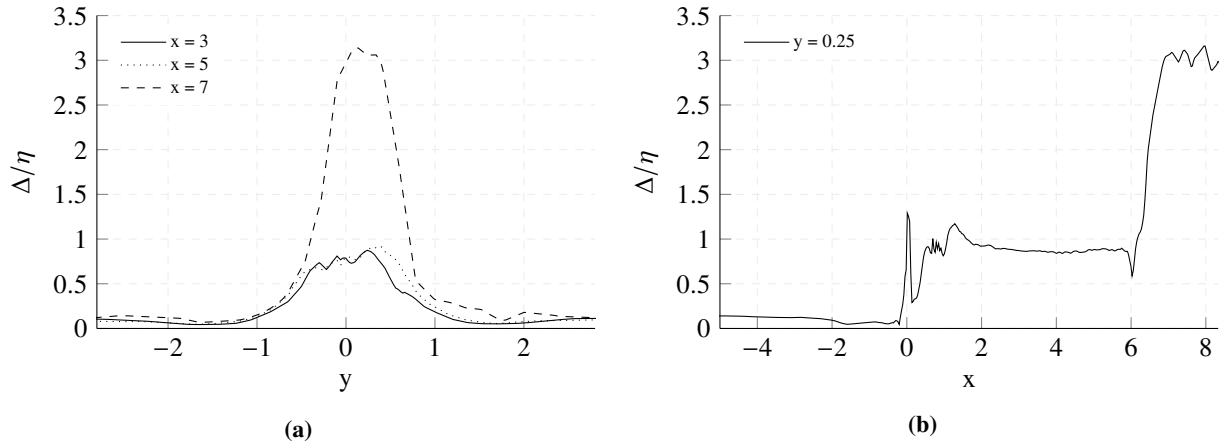

(a) (b)

Fig. 12 Plots of Δ/η in the mid-span plane as a function of y at x = 3, x = 5 and x = 7 (a) and as a function of x at y = 0.2 (b) for a representative airfoil from Group 2.

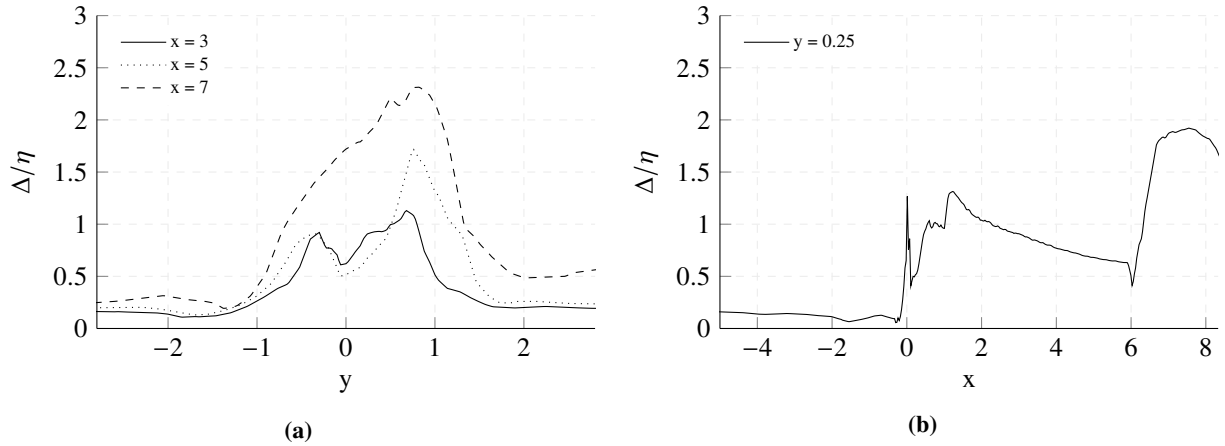

(a) (b)

Fig. 13 Plots of Δ/η in the mid-span plane as a function of y at x = 3, x = 5 and x = 7 (a) and as a function of x at y = 0.2 (b) for a representative airfoil from Group 3.

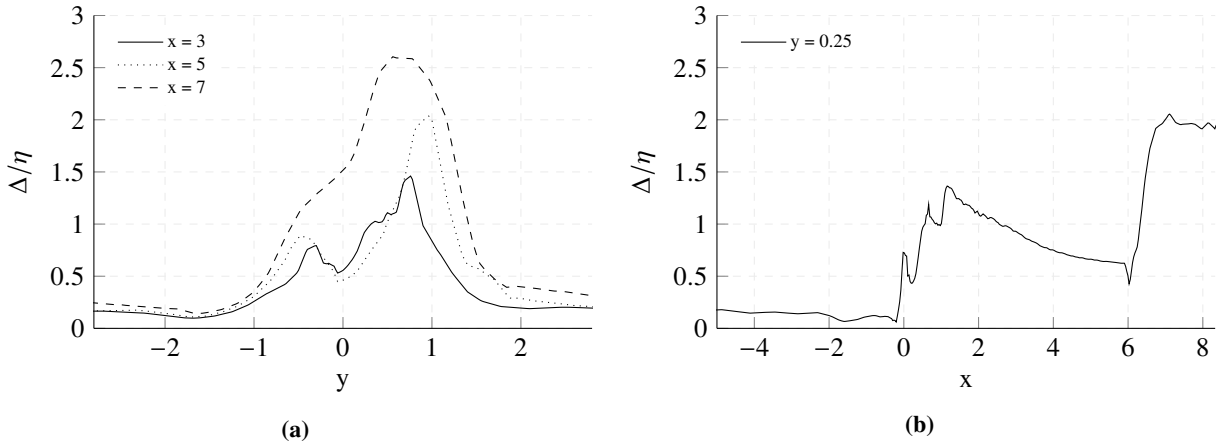

(a) (b)

Fig. 14 Plots of Δ/η in the mid-span plane as a function of y at x = 3, x = 5 and x = 7 (a) and as a function of x at y = 0.2 (b) for a representative airfoil from Group 4.